

Constraints on the Scale Parameter of Regular Black Hole in Asymptotically Safe Gravity from Extreme Mass Ratio Inspirals

Lai Zhao,¹ Meirong Tang,¹ and Zhaoyi Xu^{1,*}

¹*College of Physics, Guizhou University, Guiyang, 550025, China*

This paper evaluates the potential for constraining the quantum scale parameter ξ of regular black hole within the asymptotically safe gravity framework using gravitational waves from extreme mass ratio inspirals (EMRI). Since ξ cannot be precisely determined from first principles, observational constraints become crucial. We employ the Augmented Analytical Kludge (AAK) method to calculate gravitational waveforms in the equatorial plane and systematically analyze the influence of different ξ values on phase evolution. Comparison with the Schwarzschild case demonstrates that the corrective effects of ξ accumulate in the phase over observation time, thereby providing distinguishable observational signatures. Through waveform mismatch analysis, our results indicate that the LISA detector can effectively detect the presence of ξ at the $\sim 10^{-4}$ level for systems with a mass of $10^6 M_\odot$. Further assessment using the Fisher information matrix (FIM) confirms a measurement precision of $\Delta\xi \approx 3.225 \times 10^{-4}$, which significantly surpasses existing observational methods, providing quantitative observational evidence for asymptotically safe quantum gravity theory in the strong-field regime.

Keywords: Extreme Mass Ratio Inspirals; Gravitational Waves; Mismatch; Regular Black Hole; Fisher Information Matrix

I. INTRODUCTION

Black holes predicted by general relativity have been confirmed through gravitational wave detection [1–4] and Event Horizon Telescope observations [5–7]. However, the singularity theorems [8–10] indicate that under certain energy conditions, gravitational collapse inevitably leads to spacetime singularities, causing the failure of causal structure in those regions. To ensure spacetime completeness, one approach is the cosmic censorship conjecture [11], which proposes that singularities should be screened by event horizons, thereby protecting the causal structure of external spacetime. Another approach involves incorporating quantum gravity effects or modifying gravitational theory in the strong-field regime to suppress singularity formation, thus catalyzing the development of regular black hole models.

The regular black hole solutions are mainly obtained through two approaches: first, by introducing specific matter source terms in Einstein’s field equations to regularize the singularity. This research direction began with the pioneering regular black hole model proposed by Bardeen [12], subsequently expanded and deepened by Hayward [13] and Ayon-Beato and Garcia [14] based on different physical mechanisms, with other significant contributions in this direction seen in [15–20], and other references; The second approach is to eliminate singularities by modifying the gravitational theory framework itself, which includes two main branches: (1) modifying classical gravitational theories, such as f(R) gravity, Lovelock gravity, etc. (see, e.g., [21–25]); (2) introducing quantum effects at the semi-classical or quantum grav-

ity level to avoid singularity formation through quantum corrections (see, e.g., [26–35]).

In particular, asymptotically safe gravity in quantum gravity theory, characterized by gravitational coupling constants tending towards a non-trivial Reuter fixed point in the high-energy limit, provides a theoretically consistent and ultraviolet-complete framework capable of naturally achieving black hole singularity regularization, thus attracting widespread attention. Recently, Bonanno et al. [32], by extending Markov and Mukhanov’s ideas [36], constructed an effective Lagrangian to obtain a new type of regular black hole model. This model regulates the metric through a scale parameter ξ , which cannot be determined from first principles and can only be constrained through observations [32]. Furthermore, the influence of ξ is primarily significant at the Planck scale and has an extremely weak impact on physical behavior outside the event horizon. Therefore, in regions far from the event horizon, the physical behavior is similar to the Schwarzschild solution. Given the weak effects of ξ in the far field, observational constraints on it require gravitational field detection capabilities of extremely high precision. Future space-based gravitational wave detectors, by measuring the fine structural features of gravitational wave signals from extreme mass ratio inspirals, hold promise for effectively constraining this theoretical parameter, thereby testing the physical viability of regular black hole models under asymptotically safe gravity.

On the other hand, gravitational wave signals generated by EMRI systems formed by stellar-mass compact objects (CO) orbiting supermassive black holes at galactic centers will become one of the most promising sources for future space-based detectors (such as the Laser Interferometer Space Antenna (LISA) [37, 38], Taiji [39] and TianQin [40]). Through precise detection of these gravitational waveforms, not only can a wealth of information

* zyxu@gzu.edu.cn (Corresponding author)

about black hole spacetime structure be obtained and physical parameters measured more accurately (see e.g., [41–44]), but it also provides a real experimental platform for testing general relativity (see e.g., [45–48]). Furthermore, EMRI have made significant progress in testing the no-hair theorem and constraining parameter ranges (see e.g., [44, 49–62]). At the same time, by analyzing the modulation effects of matter distribution around supermassive black holes on gravitational waveforms, new pathways are provided for detecting black hole environments (see e.g., [63–70]). In particular, EMRI systems also have unique advantages in detecting quantum gravity effects. Small-mass bodies complete hundreds of thousands of orbital cycles in strong-field regions, significantly amplifying minute quantum effects through phase accumulation, thereby leaving characteristic imprints in the waveform (see e.g., [71–77]). This detection precision far exceeds the range achievable by other weak-field gravitational experiments, making EMRIs unique astrophysical laboratories for probing the quantum geometric microstructure of spacetime.

Based on the high-precision detection capability of EMRI systems for background spacetime structure, this study adopts the regular black hole model proposed by Bonanno et al. under the asymptotically safe gravity framework [32] as the central supermassive black hole in EMRI systems. The spacetime geometry of this black hole model is dominated by the scale parameter ξ , whose value cannot be derived from first principles and can only be constrained through observational data [32]. Discussions about ξ have been initiated in multiple domains, including quasi-normal modes [78], strong gravitational lensing effects [79], and black hole shadow observations [80]. In this paper, we focus on analyzing the leading-order effects of the parameter, first deriving the geodesic orbital frequencies, energy flux, angular momentum flux, and orbital evolution equations for a non-spinning stellar-mass compact object in the equatorial plane. Subsequently, we employ the AAK method to construct complete gravitational wave waveform templates. By calculating the phase accumulation difference relative to a Schwarzschild black hole and combining the noise characteristics of the LISA detector, we apply mismatch and Fisher information matrix analysis methods to quantitatively evaluate LISA’s measurement precision and physical constraint capabilities for ξ .

The structure of this paper is as follows: Section II introduces the black hole background and geodesics, Section III elucidates the gravitational wave construction method, including flux calculations, orbital evolution, and waveform analysis methods; Section IV presents the main research results and discussion; Section V summarizes the entire paper. Except for the data processing section, this paper adopts geometric units, i.e., $c = G = 1$.

II. REGULAR BLACK HOLE BACKGROUND AND GEODESICS IN ASYMPTOTICALLY SAFE GRAVITY

A. Background Metric

Bonanno et al. extended the ideas of Markov and Mukhanov [36] by introducing an effective Lagrangian within the asymptotically safe gravity framework to study dust collapse processes, ultimately obtaining a regular black hole model [32]. Specifically, they adopted the system action [36]

$$S = \frac{1}{16\pi G_N} \int d^4x \sqrt{-g} [R + 2\chi(\epsilon) \mathcal{L}], \quad (1)$$

where $\mathcal{L} = -\epsilon$ is the matter Lagrangian, ϵ is the fluid density, and $\chi(\epsilon)$ is a coupling function reflecting how the gravitational constant varies with energy density. Within this framework, the gravitational field equations are modified to

$$R_{\mu\nu} - \frac{1}{2}g_{\mu\nu}R = 8\pi G(\epsilon) T_{\mu\nu} - \Lambda(\epsilon) g_{\mu\nu}, \quad (2)$$

where $T_{\mu\nu} = (\epsilon + p(\epsilon))u_\mu u_\nu + pg_{\mu\nu}$ is the energy-momentum tensor, with the effective gravitational constant $G(\epsilon)$ and cosmological constant $\Lambda(\epsilon)$ given by [32]

$$8\pi G(\epsilon) = \frac{\partial(\chi\epsilon)}{\partial\epsilon}, \quad \Lambda(\epsilon) = -\epsilon^2 \frac{\partial\chi}{\partial\epsilon}. \quad (3)$$

In the theoretical framework of asymptotically safe gravity, the gravitational constant is assumed to be dominated by renormalization group trajectories approaching the ultraviolet (UV) fixed point [81–83]. Under this assumption, the gravitational constant $G(\epsilon)$ can be expressed as

$$G(\epsilon) = \frac{G_N}{1 + \xi\epsilon}, \quad (4)$$

where ξ represents the scale parameter, describing the intensity of quantum gravity corrections, whose specific magnitude needs to be constrained through observations [32].

During the process of gravitational collapse of dust (assuming a pressureless fluid with $p = 0$), asymptotically safe gravity theory predicts a regular spherically symmetric black hole solution [32], with metric

$$ds^2 = -f(r)dt^2 + f(r)^{-1}dr^2 + r^2d\Omega^2, \quad (5)$$

where

$$f(r) = 1 - \frac{r^2}{3\xi} \ln \left(1 + \frac{6M\xi}{r^3} \right). \quad (6)$$

Evidently, in the limit of $r \rightarrow 0$, this metric maintains regularity, effectively avoiding the pathological behavior caused by singularities in traditional solutions; in

the limit of scale parameter $\xi \rightarrow 0$ (or $r \rightarrow \infty$), this solution degenerates to the classical Schwarzschild black hole solution. It can be seen that asymptotically safe gravity effectively regulates gravitational behavior at high energy scales through renormalization group trajectories, thereby constructing singularity-free spacetime geometry within the theoretical framework. This characteristic demonstrates the theoretical advantages of asymptotically safe gravity theory in its self-consistency at ultra-high energy scales and its ability to avoid singularity problems.

Fig. 1 illustrates the event horizon structure of a regular black hole in asymptotically safe gravity. The left figure shows that: when $\xi < \xi_0$, metric (6) has two event horizons (inner and outer horizons); when $\xi = \xi_0$, the inner and outer horizons coincide, corresponding to an extremal black hole configuration; when $\xi > \xi_0$, metric (6) exhibits a horizon-free compact geometric structure. Notably, in regions far from the event horizon, this metric is asymptotically consistent with the Schwarzschild solution, indicating that conventional weak-field tests struggle to break this degeneracy, and detecting the effects of scale parameter ξ requires investigation in strong gravitational field regions. The right figure shows that compared to a Schwarzschild black hole, the event horizon radius of a regular black hole in asymptotically safe gravity is significantly smaller than that of a Schwarzschild black hole due to the influence of scale parameter ξ (when scale parameter $\xi \rightarrow 0$, a regular black hole in asymptotically safe gravity degenerates into a Schwarzschild black hole), a phenomenon that is a common characteristic of many regular black hole models.

B. Timelike Geodesics

In an extreme mass ratio (EMR) system, a stellar-mass CO orbiting a supermassive black hole (a regular black hole in asymptotically safe gravity) follows timelike geodesics. When the stellar-mass CO is restricted to move in the equatorial plane, i.e., $\theta = \pi/2$, the Lagrangian for the regular black hole in asymptotically safe gravity (6) is

$$\mathcal{L} = \frac{1}{2} m g_{\mu\nu} \frac{dx^\mu}{d\tau} \frac{dx^\nu}{d\tau} = \frac{1}{2} m \left(-f(r) \dot{t}^2 + \frac{1}{f(r)} \dot{r}^2 + r^2 \dot{\phi}^2 \right), \quad (7)$$

where the dot represents differentiation with respect to proper time τ . Since the black hole metric we consider is static and spherically symmetric, there exist two conserved quantities, namely the energy E and angular momentum L . At this time, the equations of motion of the system can be derived from the Lagrangian (7) as

$$\frac{dt}{d\tau} = \frac{E}{mf(r)}, \quad (8)$$

$$\left(\frac{dr}{d\tau} \right)^2 = \frac{E^2}{m^2} - f(r) \left(1 + \frac{L^2}{m^2 r^2} \right), \quad (9)$$

$$\frac{d\phi}{d\tau} = \frac{L}{mr^2}, \quad (10)$$

$$\frac{d\theta}{d\tau} = 0. \quad (11)$$

To more effectively describe the eccentric orbit of the stellar-mass CO, we parameterize the radial coordinate r with the parametric equation

$$r(\psi) = \frac{Mp}{1 + e \cos\psi}, \quad (12)$$

where p is the dimensionless semi-latus rectum and e is the orbital eccentricity. When the orbit sweeps through a complete cycle, the parameter ψ varies from 0 to 2π . The two turning points of the radial motion of the orbit can be expressed as

$$r_p = \frac{Mp}{1 + e}, \quad r_a = \frac{Mp}{1 - e}. \quad (13)$$

At these two turning points, the radial velocity of the orbit is zero, i.e., $\frac{dr}{d\tau} = 0$. Combining equations (9) and (13), the expressions for energy and angular momentum can be derived as

$$E^2 = \frac{m^2 (p - 2 - 2e)(p - 2 + 2e)}{p(p - 3 - e^2)} - \frac{m^2 (1 - e^2)^2 (p - 2 + 2e^2) \xi}{p^3 (p - 3 - e^2)^2} + O(\xi^2), \quad (14)$$

$$L^2 = -\frac{m^2 M^2 p^2}{p - 3 - e^2} - \frac{6m^2 M^2 (e^4 + 2e^2 p + 2e^2 + 2p - 3) \xi}{p(p - 3 - e^2)^2} + O(\xi^2). \quad (15)$$

Here, the scale parameter ξ has undergone a dimensionless transformation, i.e., $\xi \rightarrow M^2 \xi$. Obviously, when the scale parameter ξ vanishes, expressions (14) and (15) revert to the results for a Schwarzschild black hole [84, 85]. It is worth noting that this study aims to explore the dominant effects of the scale parameter ξ on gravitational wave signals, so we only calculate to the leading order term of the scale parameter ξ .

Since the motion of the stellar-mass CO under consideration is restricted to the equatorial plane, there exist only two fundamental frequencies: the radial frequency Ω_r and the azimuthal frequency Ω_ϕ . They are associated with radial and azimuthal motions, respectively, and can be expressed as

$$\Omega_r = \frac{2\pi}{T_r}, \quad T_r = \int_0^{t_0} dt = \int_0^{2\pi} \frac{dt}{d\psi} d\psi, \quad (16)$$

$$\Omega_\phi = \frac{\Delta\phi}{T_r}, \quad \Delta\phi = \int_0^{\phi_0} d\phi = \int_0^{2\pi} \frac{d\phi}{d\psi} d\psi. \quad (17)$$

Where T_r is the radial period and $\Delta\phi$ is the azimuthal displacement. By combining equations (8) and (10) and expanding, we can obtain

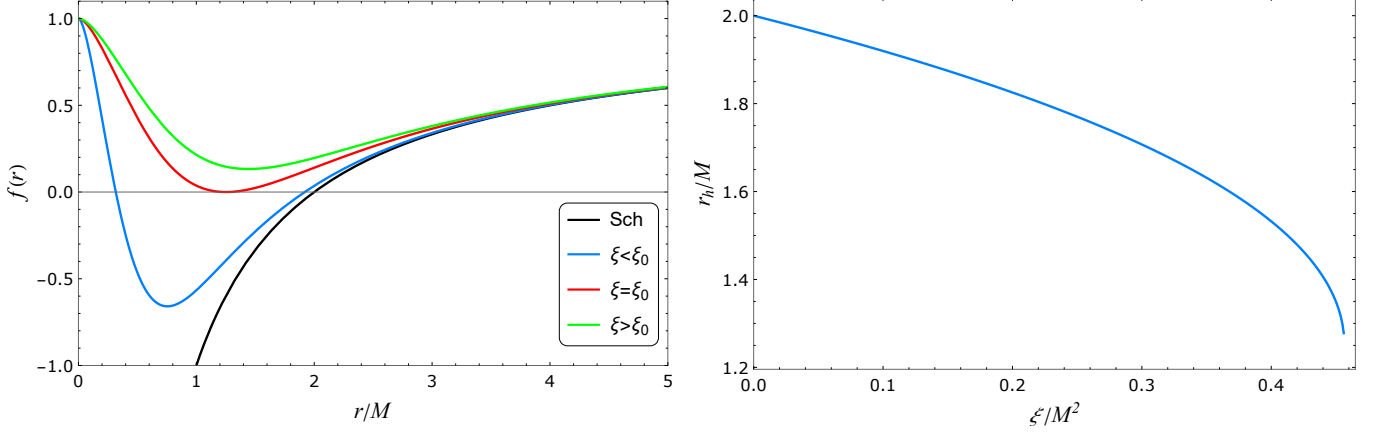


FIG. 1: The left figure shows the existence conditions for the event horizon of a regular black hole in asymptotically safe gravity, where $\frac{\xi_0}{M^2} \approx 0.4565$ represents an extremal black hole; the right figure illustrates the effect of the scale parameter ξ on the outer event horizon radius.

$$\Omega_r = \frac{X^3}{Mp^{3/2}} - \frac{3X^5}{Mp^{5/2}} - \frac{3X^5(6e^2 + 5X - 2)}{2Mp^{7/2}} - \frac{3X^5[18e^4 + 2(15X - 8)e^2 - 2(X + 3)\xi - 5X + 14]}{2Mp^{9/2}} + O(p^{-11/2}), \quad (18)$$

$$\Omega_\phi = \frac{X^3}{Mp^{3/2}} + \frac{3e^2 X^3}{Mp^{5/2}} + \frac{3X^3[12e^4 + (10X - 3)e^2 - 10(X - 1)]}{4Mp^{7/2}} + \frac{3X^3\{36e^6 + (60X - 29)e^4 - 2[(2X + 9)\xi + 20X - 39]e^2 + 4[(X - 3)\xi - 5X + 5]\}}{4Mp^{9/2}} + O(p^{-11/2}). \quad (19)$$

Where $X = \sqrt{1 - e^2}$. From expressions (14) and (15), it can be seen that the influence of the scale parameter ξ is primarily manifested in higher-order expansion terms. When $\xi = 0$, our results revert to the case of a Schwarzschild black hole.

III. METHOD

A. Flux and Orbital Evolution

In the previous section, we obtained the fundamental frequencies (Ω_r and Ω_ϕ) on the equatorial plane through geodesic analysis, but these results did not consider the effects of gravitational radiation. This section will focus on deriving orbital evolution in the regular black hole background, which is primarily driven by energy flux and angular momentum flux caused by gravitational radiation. For energy flux and angular momentum flux, we adopt expressions derived by Peters and Mathews using the standard quadrupole approximation for calculation

[86, 87], and their expressions are as follows

$$\left\langle \frac{dE}{dt} \right\rangle = \frac{1}{5}\mu \left\langle \frac{d^3 Q_{ij}}{dt^3} \frac{d^3 Q^{ij}}{dt^3} - \frac{1}{3} \frac{d^3 Q_{ii}}{dt^3} \frac{d^3 Q^{jj}}{dt^3} \right\rangle, \quad (20)$$

$$\left\langle \frac{dL_i}{dt} \right\rangle = \frac{2}{5\mu M} \epsilon_{ijk} \left\langle \frac{d^2 Q_{jm}}{dt^2} \frac{d^3 Q^{km}}{dt^3} \right\rangle. \quad (21)$$

Here, $\mu = mM/(m + M)$ is the reduced mass, which in extreme mass ratio inspiral systems can be approximated as the stellar-mass compact object, i.e., $\mu \approx m$. Q_{ij} is the inertia tensor, expressed as

$$Q_{ij} = \mu x^i x^j, \quad (22)$$

where x^i is the position vector between the stellar-mass CO and the regular black hole in asymptotically safe gravity, represented in spherical coordinates on the equatorial plane as $x^i = (r \cos \phi, r \sin \phi, 0)$. Under the weak field approximation, energy flux and angular momentum flux can be expanded as expressions containing the scale parameter. The specific forms are

$$\left\langle \frac{dE}{dt} \right\rangle = \left\langle \frac{dE}{dt} \right\rangle_{GR} + \frac{F(\xi, e)\mu^2}{M^2 p^8}, \quad (23)$$

$$\left\langle \frac{dL}{dt} \right\rangle = \left\langle \frac{dL}{dt} \right\rangle_{GR} + \frac{G(\xi, e)\mu^2}{Mp^{13/2}}. \quad (24)$$

The functions $F(\xi, e)$ and $G(\xi, e)$ represent higher-order correction terms carrying scale parameter-related contributions. Due to the complexity and length of the expressions, their specific forms are provided in Appendix A. From the structure of the formulas, it can be seen that the scale parameter ξ does not appear in the leading-order terms of p , but rather manifests its contribution in higher-order correction terms.

Orbital evolution is primarily driven by energy and angular momentum dissipation due to gravitational wave radiation. Under the adiabatic approximation, changes in the system's orbital energy and angular momentum are completely converted into energy radiated as gravitational waves, thus expressed as

$$\dot{E}_{\text{GW}} = - \left\langle \frac{dE}{dt} \right\rangle = -\mu\dot{E}, \quad (25)$$

$$\dot{L}_{\text{GW}} = - \left\langle \frac{dL}{dt} \right\rangle = -\mu\dot{L}. \quad (26)$$

Since E and L in expressions (25) and (26) are functions of p and e , chain rule differentiation yields

$$-\dot{E}_{\text{GW}} = \mu \frac{\partial E}{\partial p} \frac{dp}{dt} + \mu \frac{\partial E}{\partial e} \frac{de}{dt}, \quad (27)$$

$$-\dot{L}_{\text{GW}} = \mu \frac{\partial L}{\partial p} \frac{dp}{dt} + \mu \frac{\partial L}{\partial e} \frac{de}{dt}. \quad (28)$$

Combining expressions (27) and (28), we can obtain the orbital evolution equations ($\dot{p}(t)$ and $\dot{e}(t)$) for a stellar-mass CO in a regular black hole in asymptotically safe gravity, expressed as

$$m \frac{dp}{dt} = \left[\frac{\partial E}{\partial e} \dot{L}_{\text{GW}} - \frac{\partial L}{\partial e} \dot{E}_{\text{GW}} \right] / \left[\frac{\partial E}{\partial p} \frac{\partial L}{\partial e} - \frac{\partial E}{\partial e} \frac{\partial L}{\partial p} \right], \quad (29)$$

$$m \frac{de}{dt} = \left[\frac{\partial L}{\partial p} \dot{E}_{\text{GW}} - \frac{\partial E}{\partial p} \dot{L}_{\text{GW}} \right] / \left[\frac{\partial E}{\partial p} \frac{\partial L}{\partial e} - \frac{\partial E}{\partial e} \frac{\partial L}{\partial p} \right]. \quad (30)$$

Substituting expressions (14), (15), (23), and (24) into (29) and (30) yields the orbital evolution equations for the stellar-mass CO. Notably, orbital evolution ($\dot{p}(t)$ and $\dot{e}(t)$) will be influenced by the scale parameter ξ . Although this influence does not appear in the leading-order terms of the orbital parameter p , it regulates the evolution of higher-order terms. To intuitively present the impact of the scale parameter on orbital evolution, we analyze it by calculating the orbital evolution deviation relative to a Schwarzschild black hole, with results shown in Figure 2. Evidently, as time progresses, the orbital evolution deviations Δp , Δe between a regular black hole in asymptotically safe gravity and a Schwarzschild

black hole gradually increase, reaching maximum before the stellar-mass CO plunges into the black hole. This indicates that the influence of scale parameter ξ on orbital evolution accumulates over time, thereby providing a possibility for observational detection.

Furthermore, as the orbit evolves, the phases corresponding to the two fundamental frequencies (Ω_r, Ω_ϕ) also change, and their phase evolutions $\dot{\varphi}_r, \dot{\varphi}_\phi$ are expressed as

$$\frac{d\varphi_i}{dt} = \langle \Omega_i(p(t), e(t)) \rangle = \frac{1}{T_r} \int_0^{2\pi} \Omega_i(p(t), e(t)) \frac{dt}{d\psi} d\psi, \quad (31)$$

where $i = (r, \phi)$. To preliminarily assess the impact of scale parameter ξ on EMRI systems, we similarly employ phase deviation $\Delta\varphi_i$ at the same moment to quantify the effects of the scale parameter. The deviation is defined as $\Delta\varphi_i = \varphi_i(\xi \neq 0) - \varphi_i(\xi = 0)$.

B. Waveform Construction

In this section, we employ the AAK method to construct gravitational waveforms excited by EMRI systems. As an improved version of the Analytic Kludge (AK) method, the AAK method combines the computational efficiency of the AK method with the high-precision characteristics of the Numerical Kludge (NK) method, capable of significantly enhancing waveform accuracy while maintaining relatively low computational costs. As described in the literature [88], the AAK method can effectively increase the number of detectable EMRI events compared to the traditional AK method; while compared to the NK method, the AAK method improves computational speed by an order of magnitude. For detailed content regarding these methods, please refer to the literature [88–91].

To construct the corresponding waveforms, we adopt a coordinate system adapted to the detector, where the unit vector \hat{r} points toward the source position, and the other two unit vectors \hat{p} and \hat{q} are defined as [89]

$$\hat{p} = \frac{\hat{r} \times \hat{L}}{|\hat{r} \times \hat{L}|}, \quad \hat{q} = \hat{p} \times \hat{r}. \quad (32)$$

In the transverse-traceless gauge, the waveform is represented via the quadrupole approximation as

$$h_{ij} = \frac{2}{D_L} \left(P_{ik} P_{jl} - \frac{1}{2} P_{ij} P_{kl} \right) \ddot{I}^{kl}, \quad h^{(+,\times)} = \frac{1}{2} h_{ij} H_{ij}^{(+,\times)}. \quad (33)$$

Where D_L is the luminosity distance. The projection tensor P_{ij} is defined as $P_{ij} = \delta_{ij} - \hat{r}_i \hat{r}_j$, and the polarization basis tensors H_{ij}^+ and H_{ij}^\times are defined as

$$H_{ij}^+ = p_i p_j - q_i q_j, \quad H_{ij}^\times = p_i q_j + q_i p_j. \quad (34)$$

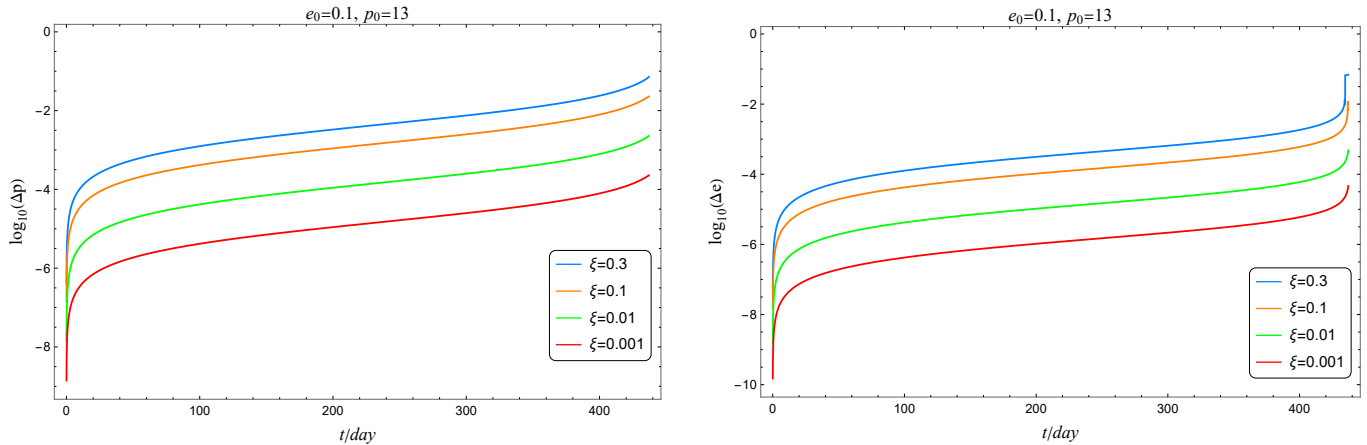


FIG. 2: The deviation $\Delta X = X_{\xi \neq 0} - X_{\xi=0}$ in the semi-latus rectum p and eccentricity e over time evolution under different scale parameters ξ , where $X = \{p, e\}$. The corresponding initial conditions are $p_0 = 13, e_0 = 0.1$.

The gravitational waveform can be represented as a superposition of n -th harmonic components

$$h^+ = A \sum_n h_n^+, \quad h^\times = A \sum_n h_n^\times, \quad (35)$$

where $A = \frac{(M\Omega_\phi)^{2/3}m}{D_L}$, and the expressions for h_n^+ and h_n^\times are [89]

$$h_n^+ = \left[1 + (\hat{r} \cdot \hat{L})^2 \right] [b_n \sin(2\gamma) - a_n \cos(2\gamma)] + \left[1 - (\hat{r} \cdot \hat{L})^2 \right] c_n, \quad (36)$$

$$h_n^\times = 2 (\hat{r} \cdot \hat{L}) [b_n \cos(2\gamma) + a_n \sin(2\gamma)]. \quad (37)$$

Where $\gamma = \Phi_\phi - \Phi_r$ represents the azimuthal angle, and coefficients $a_n, b_n,$ and c_n can be expressed through Bessel functions of the first kind [89].

Within the LISA detector framework, the two polarized gravitational wave signals are transformed into detector measurement outputs via specific response functions, specifically given as

$$h^{I,II}(t) = \frac{\sqrt{3}}{2} \left[h_+(t) F_+^{I,II}(t) + h_\times(t) F_\times^{I,II}(t) \right]. \quad (38)$$

Where $F_+^{I,II}(t)$ and $F_\times^{I,II}(t)$ are the LISA antenna pattern functions, which depend on the geometric configuration of the source direction (θ_S, ϕ_S) and black hole spin direction (θ_K, ϕ_K) in the ecliptic coordinate system [89, 92, 93].

C. Mismatch and Fisher Information Matrix

To quantify the effect of the scale parameter ξ on the waveform, we compare the overlap between the regular

black hole waveform signal with $\xi \neq 0$ and the traditional black hole waveform with $\xi = 0$. The overlap $\mathcal{O}(h_a|h_b)$ is defined as

$$\mathcal{O}(h_a|h_b) = \frac{\langle h_a|h_b \rangle}{\sqrt{\langle h_a|h_a \rangle \langle h_b|h_b \rangle}}. \quad (39)$$

Where the noise-weighted inner product $\langle h_a|h_b \rangle$ is

$$\langle h_a|h_b \rangle = 2 \int_0^\infty df \frac{h_a^*(f) h_b(f) + h_a(f) h_b^*(f)}{S_n(f)}. \quad (40)$$

Here, $h_{a,b}(f)$ is the Fourier transform of the time-domain signal. S_n is the noise power spectral density of the detector, such as LISA [94, 95], TianQin [96], and Taiji [97].

Based on the definition of overlap, the mismatch \mathcal{M} can be directly expressed as

$$\mathcal{M} = 1 - \mathcal{O}(h_a | h_b). \quad (41)$$

When two signals are identical, the overlap is $\mathcal{O} = 1$ and the mismatch is $\mathcal{M} = 0$. As described in the literature [77, 98, 99], to effectively distinguish between two waveform signals, the mismatch must satisfy $\mathcal{M} \geq D/2\rho^2$, where ρ is the signal-to-noise ratio and D represents the number of intrinsic parameters in the system. In this paper, there are only six intrinsic parameters. For EMRI systems, the LISA detection threshold is typically set at a signal-to-noise ratio of 20 [41]. Therefore, the mismatch threshold for distinguishing gravitational wave signals from regular black holes in asymptotically safe gravity is $\mathcal{M} = 0.0075$.

To further evaluate LISA's capability to measure the scale parameter, we employ the FIM to assess the accuracy of parameter estimation at a relatively high signal-to-noise ratio [100]. The FIM is defined as follows

$$\Gamma_{ij} = \left\langle \frac{\partial h}{\partial \lambda_i} \middle| \frac{\partial h}{\partial \lambda_j} \right\rangle, \quad (42)$$

where λ_i represents the set of relevant parameters that constitute the gravitational wave signal (38). Under high SNR conditions, the variance-covariance matrix for parameter estimation can be approximated using the inverse of the FIM, namely

$$\Sigma_{ij} \equiv \langle \delta\lambda_i \delta\lambda_j \rangle = (\Gamma^{-1})_{ij}. \quad (43)$$

The statistical uncertainty for a specific parameter is given by the square root of the diagonal elements of the variance-covariance matrix (43)

$$\sigma_i = \Sigma_{ii}^{1/2} \quad (44)$$

The space-based gravitational wave detectors, represented by LISA, adopt a dual-channel interferometer design, achieving high-precision waveform reconstruction through joint measurement data from both channels. In this multi-channel framework, the calculation of signal-to-noise ratio and covariance matrix should consider the contributions from these two channels. Specifically, the total system signal-to-noise ratio can be expressed as [67, 75]

$$\rho = \sqrt{\langle h_1|h_1 \rangle + \langle h_2|h_2 \rangle} \quad (45)$$

The diagonal elements of the covariance matrix are

$$\sigma_i^2 = (\Gamma_1 + \Gamma_2)_{ii}^{-1} \quad (46)$$

IV. RESULTS

In this section, to demonstrate the differences between gravitational wave signals from a regular black hole in asymptotically safe gravity and a traditional black hole, we set the parameter configuration: observation time of one year, $M = 10^6 M_\odot$, $m = 10 M_\odot$, $D_L = 1$ Gpc, $\theta_s = \frac{\pi}{3}$, $\phi_s = \frac{\pi}{2}$, $\theta_1 = \frac{\pi}{4}$, $\phi_1 = \frac{\pi}{4}$. The initial orbital parameters e_0 and p_0 are marked in the corresponding figures. When selecting p_0 , we ensure that the inspiral process during the observation period always remains far from the truncation point of the last stable orbit [101], thereby guaranteeing that the waveform evolution can fully continue for one year. Based on these parameters, we performed numerical evolution of the gravitational wave signals and compared the differences in waveform characteristics between the regular black hole and the traditional black hole. To evaluate the detectability of the scale parameter, we applied mismatch analysis and the FIM method to quantify waveform differences and provide theoretical predictions for scale parameter estimation precision.

A. Waveform and Mismatch

Figure 3 presents the impact of the scale parameter ξ on the gravitational waveform h^+ , evolving under initial eccentricity conditions of $e_0 = 0.1$ and $e_0 = 0.3$.

All waveforms begin their evolution from identical initial conditions, with the left column showing the waveform in the early evolution stage and the right column showing the waveform after 120 days of evolution. The black curves represent the Schwarzschild black hole ($\xi = 0$) waveform, while the blue dashed lines and red dashed lines correspond to the regular black hole waveforms with scale parameters $\xi = 0.01$ and $\xi = 0.001$, respectively. The results indicate that during the early evolution stage, the waveforms under different scale parameters almost completely overlap. However, as time progresses, the correction effects introduced by the scale parameter in the regular black hole gradually accumulate, leading to significantly increased differences in the waveforms. The larger the value of scale parameter ξ , the more pronounced the deviation in the waveform.

In Figures 4 and 5, we calculate the phase difference between the regular black hole and the Schwarzschild black hole by numerically solving equation (31), defined as $\Delta\varphi_i = \varphi_i(\xi \neq 0) - \varphi_i(\xi = 0)$, with all initial phases set to $\varphi_i|_{t=0} = 0$. Figure 4 fixes the initial conditions $e_0 = 0.1$ and $p_0 = 13$, showing the evolution of phase differences over time under different scale parameters; Figure 5 fixes the scale parameter $\xi = 0.01$ and $p_0 = 13$, showing the time evolution of phase differences under different initial eccentricities. According to the literature [77, 102, 103], when the phase difference exceeds 1 radian (black horizontal line in the figures), LISA can effectively distinguish between these two signals. Evidently, both the radial and azimuthal phase differences increase monotonically with time, eventually exceeding LISA's detection threshold. Figure 4 indicates that under fixed initial eccentricity conditions, larger scale parameters lead to more rapid growth in phase differences. Even when the scale parameter is only of the order of 10^{-3} , the phase difference after several months can reach LISA's resolution threshold, providing a preliminary basis for constraining the scale parameter. Figure 5 shows that under fixed scale parameter conditions, the initial eccentricity has a relatively minor impact on the phase difference. Overall, the influence of the scale parameter on the phase difference is significantly greater than that of the initial eccentricity.

Figure 6 quantitatively demonstrates the mismatch between the waveforms of the regular black hole in asymptotically safe gravity and the traditional black hole, with an observation time of one year. The results indicate that as the scale parameter ξ increases, the waveform mismatch gradually increases and eventually exceeds the identification threshold of the LISA detector (the red dashed line represents LISA's detection threshold). At larger scale parameters, the mismatch approaches 1. The left panel of Figure 6 shows that under fixed other parameters, the effect of eccentricity on the mismatch is relatively small, which is consistent with the phase difference analysis results in Figure 5. The right panel of Figure 6 displays the mismatch under different masses of the primary black hole, indicating that systems with

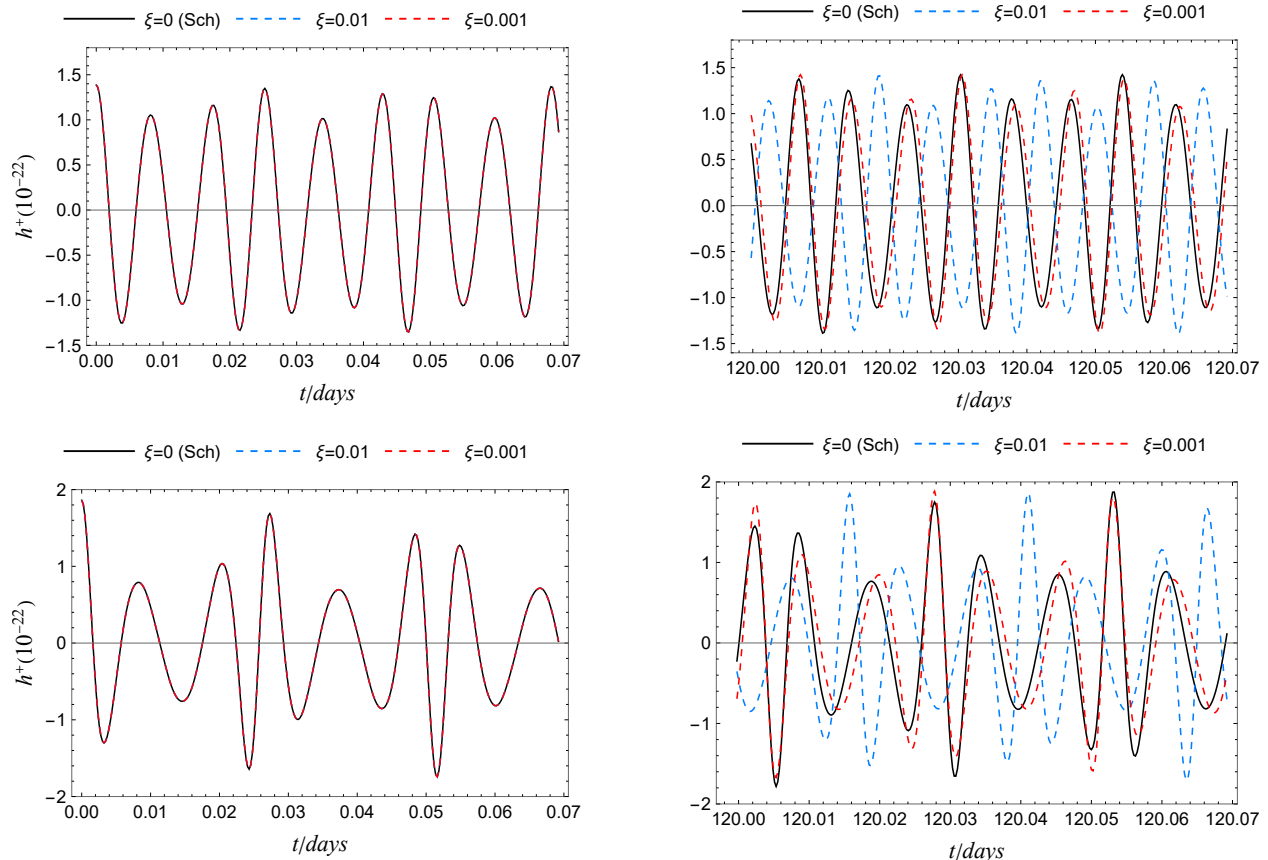


FIG. 3: Initial conditions are set to $e_0 = 0.1$ (first row of figures), $e_0 = 0.3$ (second row of figures), and $p_0 = 13$, to study the effects of different scale parameters ξ on gravitational waveforms. The black curves represent the gravitational waveforms of the Schwarzschild black hole ($\xi = 0$), while the colored curves represent the gravitational waveforms of the regular black hole in the asymptotically safe gravity framework, with scale parameters $\xi = 0.01$ (blue dashed lines) and $\xi = 0.001$ (red dashed lines). The left column shows the waveforms at the early stage of evolution, and the right column shows the waveforms after 120 days of evolution.

smaller mass black holes more easily reach the detection threshold. Comprehensive analysis shows that for systems with a mass of $10^6 M_\odot$, LISA's detection capability for the scale parameter ξ during a one-year observation period can reach the order of $\sim 10^{-4}$, suggesting that the constraint precision may also approach this magnitude, a precision that cannot be achieved by other observational methods. This is primarily attributed to the cumulative effects produced by the spacetime metric corrections induced by the scale parameter during the long-term evolution of the gravitational wave phase.

B. Constraints on the Scale Parameter

To further quantify the measurement precision of the scale parameter, in this subsection we employ the FIM

method for parameter uncertainty analysis. The FIM provides the optimal statistical precision attainable under given observational conditions and is an effective tool for evaluating parameter constraint capabilities. To ensure the robustness of the analysis results, we control the signal-to-noise ratio at approximately 50 by adjusting the system's luminosity distance, which both guarantees sufficient statistical significance of the signal and avoids non-Gaussian effects that might be introduced by excessively high signal-to-noise ratios. In our calculations, we set the scale parameter to $\xi = 0$ (i.e., the value expected in general relativity), while fixing other physical parameters (such as M , m , p_0 , and e_0).

Figure 7 displays the joint posterior probability distribution across multiple parameters, including the correlation structure between the scale parameter ξ and other key parameters, as well as their marginal proba-

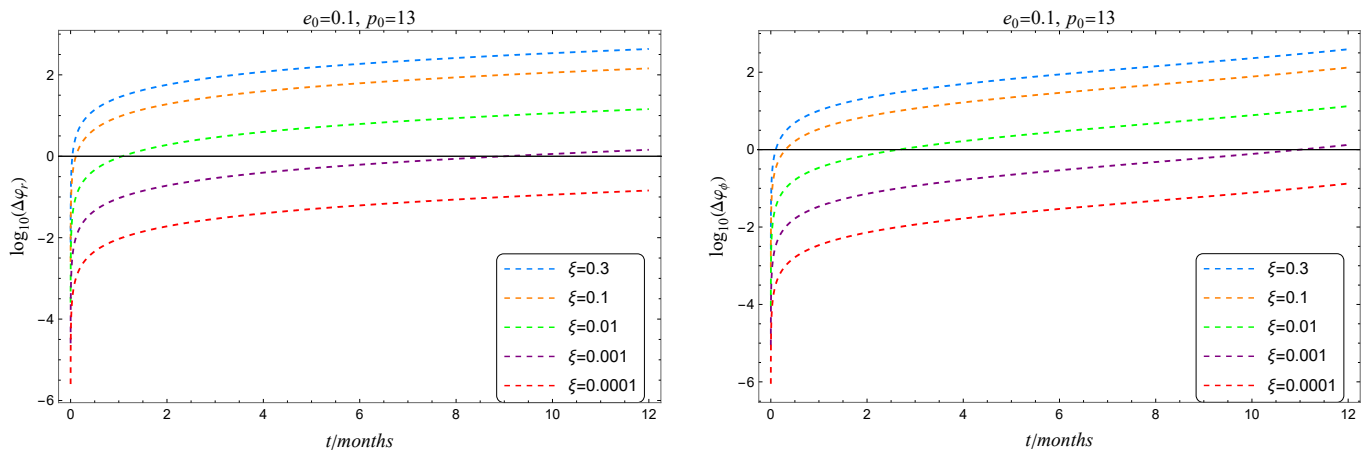


FIG. 4: Under fixed conditions of $e_0 = 0.1$ and $p_0 = 13$, the evolution of phase differences over time for different scale parameters ξ is shown. The left panel displays the radial phase difference, and the right panel shows the azimuthal phase difference, where the phase difference is defined as $\Delta\varphi_i = \varphi_i(\xi \neq 0) - \varphi_i(\xi = 0)$. The black horizontal line in the figures represents the phase threshold that can be distinguished by detection.

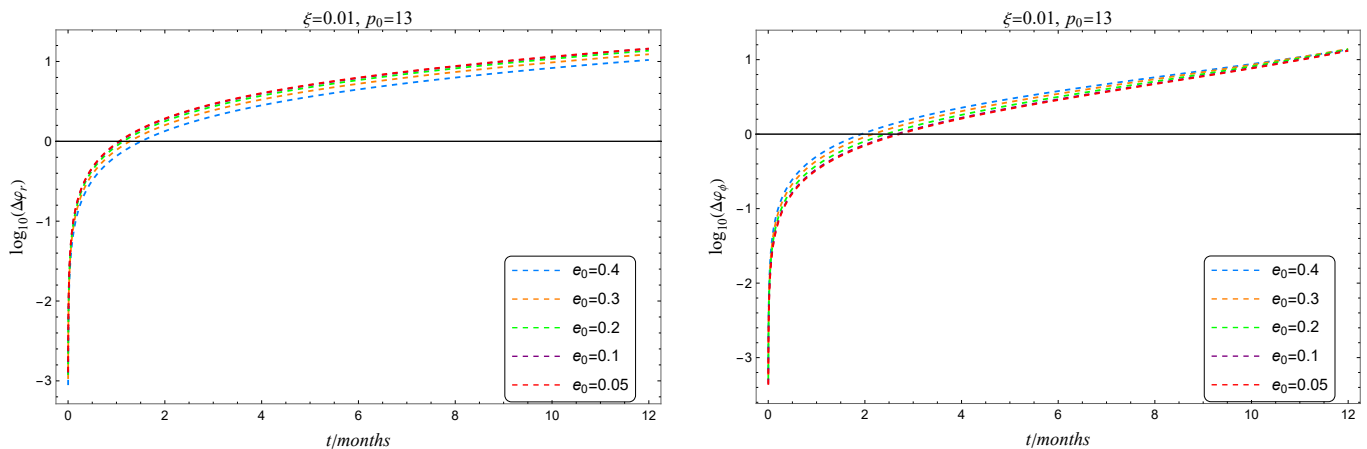


FIG. 5: Under fixed scale parameter $\xi = 0.01$, the evolution of phase differences over time for different eccentricities e_0 is shown. The left panel displays the radial phase difference, and the right panel shows the azimuthal phase difference, where the phase difference is defined as $\Delta\varphi_i = \varphi_i(\xi \neq 0) - \varphi_i(\xi = 0)$. The black horizontal line in the figures represents the phase threshold that can be distinguished by detection.

bility distributions. The analysis indicates that within a one-year LISA observation period, the theoretical 1σ measurement precision for the scale parameter can reach $\Delta\xi \approx 3.225 \times 10^{-4}$. This constraint precision is at a level that cannot be achieved by other existing observational methods. Therefore, gravitational wave signals produced by extreme mass ratio inspirals possess unique advantages in testing the characteristics of regular black holes within the asymptotically safe gravity framework.

To evaluate the numerical reliability of the above results, we conducted systematic stability tests following the standard methods in the literature [104]. Specifically,

we applied perturbations of two scales, namely $\pm 10^{-6}$ and $\pm 10^{-9}$, respectively, to evaluate the stability of the system. The results show that under $\pm 10^{-6}$ scale perturbations, the system stability is 4.364×10^{-4} ; under $\pm 10^{-9}$ scale perturbations, the system stability is 4.386×10^{-7} . These systematic test results strongly support the reliability and robustness of our main analytical conclusions.

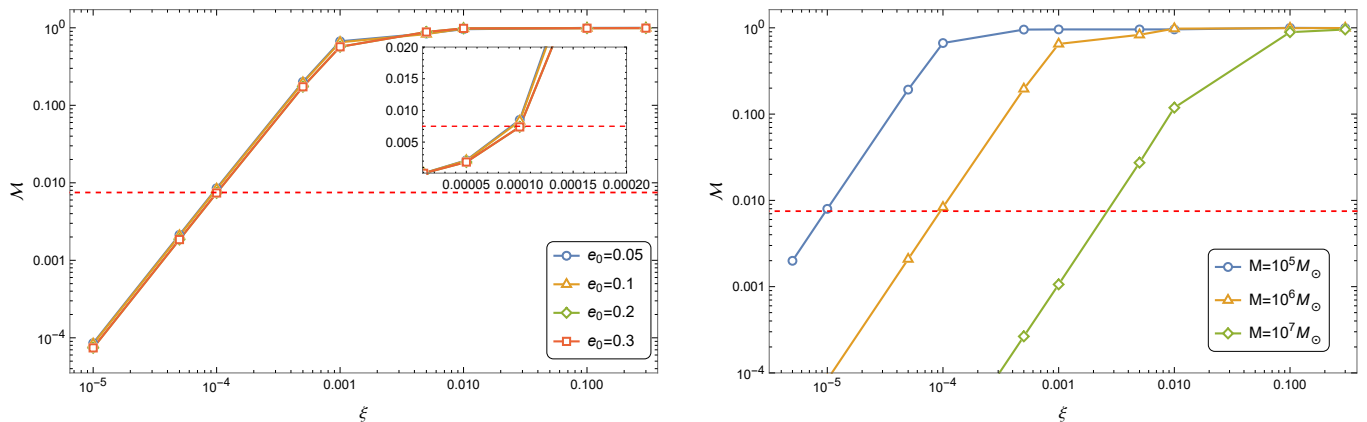


FIG. 6: With one year of evolution time, the figure shows the waveform mismatch between the regular black hole in asymptotically safe gravity and the Schwarzschild black hole. The left panel displays the waveform mismatch under fixed other parameters for eccentricities $e_0 \in \{0.05, 0.1, 0.2, 0.3\}$; the right panel shows the waveform mismatch under fixed other parameters for masses $M \in \{10^5 M_\odot, 10^6 M_\odot, 10^7 M_\odot\}$. The red dashed line represents LISA detector's minimum identification threshold $\mathcal{M} = 0.0075$.

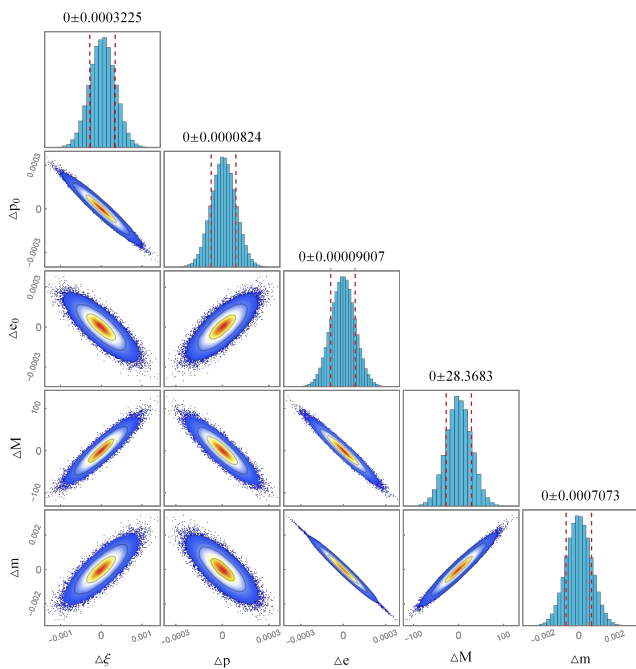


FIG. 7: Probability distribution diagram of intrinsic parameters in extreme mass ratio inspiral systems. The scale parameter $\xi = 0$, red dashed lines indicate the first confidence interval, and contours from outer to inner correspond to 99%, 95%, and 68% probability distribution regions, respectively.

V. CONCLUSION

This paper investigates the regular black hole model proposed by Bonanno et al. [32] within the asymp-

totically safe gravity framework. This model modifies the Misner-Sharp mass function to $M(r) = \frac{r^3}{6\xi} \log\left(1 + \frac{6M_0\xi}{r^3}\right)$ by introducing a gravity-matter coupling function χ , thereby eliminating the singularity at the center of classical black holes. The scale parameter ξ cannot be precisely determined from first principles, thus requiring constraints from astronomical observations. Based on this, we used the AAK method to approximately calculate the gravitational wave characteristics produced by this regular black hole model in EMRI systems on the equatorial plane. By quantifying the phase accumulation shift caused by quantum gravity effects, we assessed the potential constraint capability of gravitational wave observations on ξ , providing theoretical basis for verifying the effectiveness of asymptotically safe quantum gravity theory in the strong-field regime.

Specifically, we rigorously derived the energy and angular momentum fluxes, fundamental orbital frequencies, and orbital evolution equations on the equatorial plane. To evaluate the influence of the scale parameter, we rigorously calculated the leading-order contribution of ξ , finding that the effects of ξ are primarily manifested in higher-order terms. Subsequently, we constructed complete gravitational wave waveform templates using the AAK method.

Through systematic comparison of phase differences between waveforms of this model and Schwarzschild black hole, we quantitatively assessed the constraint capability on the scale parameter. We constructed gravitational wave waveforms for scale parameters $\xi = 0$ (Schwarzschild black hole), $\xi = 0.01$, and $\xi = 0.001$ under different initial eccentricity conditions. Results show that after several months of observation period, the waveforms exhibit significant differences, with larger ξ val-

ues highlighting differences earlier. This conclusion was rigorously verified in phase deviation analysis: larger ξ values more easily exceed the phase detection threshold, while eccentricity has no significant impact on phase deviation.

Additionally, by calculating the mismatch between waveforms with scale parameter corrections and Schwarzschild black hole waveforms, good constraints on ξ can be obtained within the LISA detection threshold. For example, for EMRI systems with $M = 10^6 M_\odot$, LISA gravitational wave observations can detect scale parameters ξ on the order of $\sim 10^{-4}$, a constraint precision significantly superior to all other current astronomical observation methods. Finally, we applied the FIM method to rigorously evaluate the measurement error of ξ . Results indicate that under $M = 10^6 M_\odot$, the measurement precision of LISA detector for ξ is $\Delta\xi \approx 3.225 \times 10^{-4}$, providing observable experimental verification evidence for asymptotically safe gravity theory.

Our research preliminarily explores the potential of using EMRI systems to constrain the scale parameter in asymptotically safe gravity theory. Subsequent work can improve waveform template precision by implementing complete black hole perturbation theory methods and incorporating higher-order radiation multipole contributions, thereby more accurately characterizing the characteristic structure of quantum gravity effects in the strong-field limit and imposing more stringent observational constraints on the scale parameter.

VI. ACKNOWLEDGEMENTS

We acknowledge the anonymous referee for a constructive report that has significantly improved this paper. This work was supported by Guizhou Provin-

cial Basic Research Program(Natural Science)(Grant No. QianKeHeJiChu-[2024]Young166), the Special Natural Science Fund of Guizhou University (Grant No.X2022133), the National Natural Science Foundation of China (Grant No. 12365008) and the Guizhou Provincial Basic Research Program (Natural Science) (Grant No. QianKeHeJiChu-ZK[2024]YiBan027) .

Appendix A: Energy Flux and Angular Momentum Flux Derivation

In this appendix, we start from the classical flux formula derived by Peters and Mathews [86, 87] and provide a detailed derivation of the gravitational wave flux expression required in this paper.

The flux formula derived by Peters and Mathews is

$$\left\langle \frac{dE}{dt} \right\rangle = \frac{1}{5} \mu \left\langle \frac{d^3 Q_{ij}}{dt^3} \frac{d^3 Q^{ij}}{dt^3} - \frac{1}{3} \frac{d^3 Q_{ii}}{dt^3} \frac{d^3 Q^{jj}}{dt^3} \right\rangle, \quad (\text{A1})$$

$$\left\langle \frac{dL_i}{dt} \right\rangle = \frac{2}{5\mu M} \epsilon_{ijk} \left\langle \frac{d^2 Q_{jm}}{dt^2} \frac{d^3 Q^{km}}{dt^3} \right\rangle. \quad (\text{A2})$$

The moment of inertia tensor Q_{ij} is

$$Q_{ij} = \mu x^i x^j. \quad (\text{A3})$$

Here, x^i represents the position vector between the stellar-mass CO and the regular black hole in asymptotically safe gravity.

To study the effect of the scale parameter on gravitational wave radiation, we only calculate up to the leading order term in the scale parameter. Therefore, the energy flux can be expressed as

$$\begin{aligned} \left\langle \frac{dE}{dt} \right\rangle &= \frac{X^3(37e^4 + 292e^2 + 96)\mu^2}{15M^2p^5} + \frac{e^2 X^3(53e^4 + 450e^2 + 176)\mu^2}{5M^2p^6} \\ &+ \frac{X^3 [2160e^8 + (456 - 5880X)e^2 - 2880(X - 1) + (1110X + 13559)e^6 + 18(425X - 728)e^4] \mu^2}{60M^2p^7} \\ &+ \frac{F(\xi, e)\mu^2}{M^2p^8} + O(1/p^9). \end{aligned} \quad (\text{A4})$$

The angular momentum flux is

$$\begin{aligned} \left\langle \frac{dL}{dt} \right\rangle &= \frac{4X^3(8 + 7e^2)\mu^2}{5Mp^{7/2}} + \frac{4e^2 X^3(38 + 27e^2)\mu^2}{5Mp^{9/2}} \\ &+ \frac{3X^3 [207e^6 + 4(5X - 33)e^2 - 160(X - 1) + (140X + 43)e^4] \mu^2}{10Mp^{11/2}} + \frac{G(\xi, e)\mu^2}{Mp^{13/2}} + O(1/p^{15/2}). \end{aligned} \quad (\text{A5})$$

Here, $X = \sqrt{1 - e^2}$, where $F(\xi, e)$ and $G(\xi, e)$ are correction functions containing the scale parameter, with specific

expressions given by

$$\begin{aligned}
F(\xi, e) = X^3 \left\{ 108e^{10} + \frac{502739e^8}{1280} - \frac{17104e^7}{275} - \frac{71469783e^6}{12800} + \frac{1757936e^5}{1225} - \frac{177180337e^4}{6144} + \frac{764430272e^3}{30625} \right. \\
- \frac{971493e^2}{32} + \frac{14148672e}{625} - \frac{23037}{5} + X (135e^8 + 1015e^6 - 450e^4 - 604e^2 - 96) \\
+ \pi^2 \left(\frac{3093e^6}{20} + \frac{384633e^4}{80} - \frac{27072e^3}{25} + 14019e^2 - \frac{19008e}{25} + \frac{18144}{5} \right) \\
\left. + \left[\frac{337e^6}{10} + \frac{4084e^4}{5} + \frac{10748e^2}{5} + X \left(-\frac{37e^6}{5} - 51e^4 + \frac{196e^2}{5} + \frac{96}{5} \right) + \frac{2208}{5} \right] \xi \right\}, \quad (A6)
\end{aligned}$$

$$\begin{aligned}
G(\xi, e) = X^3 \left\{ \frac{1863e^8}{10} - \frac{12e^7}{5} - \frac{99351e^6}{640} - \frac{57324e^5}{175} - \frac{5360461e^4}{1280} - \frac{1763028e^3}{6125} - \frac{51159e^2}{4} + \frac{1244388e}{125} - \frac{18069}{5} \right. \\
+ X (288e^6 + 168e^4 - 360e^2 - 96) + \pi^2 \left(\frac{3231e^4}{10} + \frac{24528e^2}{5} + \frac{17568}{5} \right) \\
\left. + \left[636e^2 + X \left(-\frac{84e^4}{5} - \frac{12e^2}{5} + \frac{96}{5} \right) + \frac{1824}{5} \right] \xi \right\}. \quad (A7)
\end{aligned}$$

-
- [1] B. P. Abbott *et al.* (LIGO Scientific, Virgo), *Phys. Rev. Lett.* **116**, 131103 (2016), arXiv:1602.03838 [gr-qc].
- [2] B. P. Abbott *et al.* (LIGO Scientific, Virgo), *Phys. Rev. Lett.* **116**, 061102 (2016), arXiv:1602.03837 [gr-qc].
- [3] B. P. Abbott *et al.* (LIGO Scientific, Virgo), *Phys. Rev. X* **9**, 031040 (2019), arXiv:1811.12907 [astro-ph.HE].
- [4] B. P. Abbott *et al.* (LIGO Scientific, Virgo), *Astrophys. J. Lett.* **892**, L3 (2020), arXiv:2001.01761 [astro-ph.HE].
- [5] K. Akiyama *et al.* (Event Horizon Telescope), *Astrophys. J. Lett.* **875**, L1 (2019), arXiv:1906.11238 [astro-ph.GA].
- [6] K. Akiyama *et al.* (Event Horizon Telescope), *Astrophys. J. Lett.* **930**, L12 (2022), arXiv:2311.08680 [astro-ph.HE].
- [7] R. Genzel, F. Eisenhauer, and S. Gillessen, *Rev. Mod. Phys.* **82**, 3121 (2010), arXiv:1006.0064 [astro-ph.GA].
- [8] R. Penrose, *Phys. Rev. Lett.* **14**, 57 (1965).
- [9] S. W. Hawking and R. Penrose, *Proc. Roy. Soc. Lond. A* **314**, 529 (1970).
- [10] J. M. M. Senovilla, *Gen. Rel. Grav.* **30**, 701 (1998), arXiv:1801.04912 [gr-qc].
- [11] R. Penrose, *Riv. Nuovo Cim.* **1**, 252 (1969).
- [12] J. Bardeen, in *Proceedings of the 5th International Conference on Gravitation and the Theory of Relativity* (1968) p. 87.
- [13] S. A. Hayward, *Phys. Rev. Lett.* **96**, 031103 (2006), arXiv:gr-qc/0506126.
- [14] E. Ayon-Beato and A. Garcia, *Phys. Rev. Lett.* **80**, 5056 (1998), arXiv:gr-qc/9911046.
- [15] I. Dymnikova, *Gen. Rel. Grav.* **24**, 235 (1992).
- [16] K. A. Bronnikov and J. C. Fabris, *Phys. Rev. Lett.* **96**, 251101 (2006), arXiv:gr-qc/0511109.
- [17] Z.-Y. Fan and X. Wang, *Phys. Rev. D* **94**, 124027 (2016), arXiv:1610.02636 [gr-qc].
- [18] F. S. N. Lobo, M. E. Rodrigues, M. V. de Sousa Silva, A. Simpson, and M. Visser, *Phys. Rev. D* **103**, 084052 (2021), arXiv:2009.12057 [gr-qc].
- [19] Z. Xu and M. Tang, *Eur. Phys. J. C* **81**, 863 (2021), arXiv:2109.13813 [gr-qc].
- [20] J. Ovalle, R. Casadio, and A. Giusti, *Phys. Lett. B* **844**, 138085 (2023), arXiv:2304.03263 [gr-qc].
- [21] P. Bueno, P. A. Cano, and R. A. Hennigar, *Phys. Lett. B* **861**, 139260 (2025), arXiv:2403.04827 [gr-qc].
- [22] J. T. S. S. Junior and M. E. Rodrigues, *Eur. Phys. J. C* **83**, 475 (2023), arXiv:2306.04661 [gr-qc].
- [23] A. Bakopoulos, C. Charmousis, P. Kanti, N. Lecoeur, and T. Nakas, *Phys. Rev. D* **109**, 024032 (2024), arXiv:2310.11919 [gr-qc].
- [24] J. C. Fabris, E. L. B. Junior, and M. E. Rodrigues, *Eur. Phys. J. C* **83**, 884 (2023), arXiv:2310.00714 [gr-qc].
- [25] M. Estrada and R. Aros, *JCAP* **01**, 032 (2025), arXiv:2409.09559 [gr-qc].
- [26] C. G. Boehmer and K. Vandersloot, *Phys. Rev. D* **76**, 104030 (2007), arXiv:0709.2129 [gr-qc].
- [27] R. Casadio, A. Giusti, and J. Ovalle, *JHEP* **05**, 118 (2023), arXiv:2303.02713 [gr-qc].
- [28] P. Nicolini, E. Spallucci, and M. F. Wondrak, *Phys. Lett. B* **797**, 134888 (2019), arXiv:1902.11242 [gr-qc].
- [29] B. Knorr and A. Platania, *Phys. Rev. D* **106**, L021901 (2022), arXiv:2202.01216 [hep-th].
- [30] J. Brannlund, S. Kloster, and A. DeBenedictis, *Phys. Rev. D* **79**, 084023 (2009), arXiv:0901.0010 [gr-qc].
- [31] J. Lewandowski, Y. Ma, J. Yang, and C. Zhang, *Phys. Rev. Lett.* **130**, 101501 (2023), arXiv:2210.02253 [gr-qc].
- [32] A. Bonanno, D. Malafarina, and A. Panassiti, *Phys. Rev. Lett.* **132**, 031401 (2024), arXiv:2308.10890 [gr-qc].
- [33] A. Akil, M. Cadoni, L. Modesto, M. Oi, and A. P. Sanna, *Phys. Rev. D* **108**, 044051 (2023), arXiv:2211.01657 [gr-qc].

- [34] A. Bonanno and M. Reuter, *Phys. Rev. D* **62**, 043008 (2000), arXiv:hep-th/0002196.
- [35] J. M. Pawłowski and J. Tränkle, *Phys. Rev. D* **110**, 086011 (2024), arXiv:2309.17043 [hep-th].
- [36] M. A. Markov and V. F. Mukhanov, *Nuovo Cim. B* **86**, 97 (1985).
- [37] K. Danzmann, *Class. Quant. Grav.* **14**, 1399 (1997).
- [38] P. Amaro-Seoane *et al.* (LISA), (2017), arXiv:1702.00786 [astro-ph.IM].
- [39] W.-R. Hu and Y.-L. Wu, *Natl. Sci. Rev.* **4**, 685 (2017).
- [40] J. Luo *et al.* (TianQin), *Class. Quant. Grav.* **33**, 035010 (2016), arXiv:1512.02076 [astro-ph.IM].
- [41] S. Babak, J. Gair, A. Sesana, E. Barausse, C. F. Sopuerta, C. P. L. Berry, E. Berti, P. Amaro-Seoane, A. Petiteau, and A. Klein, *Phys. Rev. D* **95**, 103012 (2017), arXiv:1703.09722 [gr-qc].
- [42] C. P. L. Berry, S. A. Hughes, C. F. Sopuerta, A. J. K. Chua, A. Heffernan, K. Holley-Bockelmann, D. P. Mihaylov, M. C. Miller, and A. Sesana, (2019), arXiv:1903.03686 [astro-ph.HE].
- [43] H.-M. Fan, Y.-M. Hu, E. Barausse, A. Sesana, J.-d. Zhang, X. Zhang, T.-G. Zi, and J. Mei, *Phys. Rev. D* **102**, 063016 (2020), arXiv:2005.08212 [astro-ph.HE].
- [44] T.-G. Zi, J.-D. Zhang, H.-M. Fan, X.-T. Zhang, Y.-M. Hu, C. Shi, and J. Mei, *Phys. Rev. D* **104**, 064008 (2021), arXiv:2104.06047 [gr-qc].
- [45] P. Shen, Q. Cui, and W.-B. Han, *Phys. Rev. D* **111**, 024004 (2025), arXiv:2501.07264 [gr-qc].
- [46] S. Kumar, in *17th Marcel Grossmann Meeting: On Recent Developments in Theoretical and Experimental General Relativity, Gravitation, and Relativistic Field Theories* (2024) arXiv:2410.08544 [gr-qc].
- [47] S. Kumar, R. K. Singh, A. Chowdhuri, and A. Bhat-tacharyya, *JCAP* **10**, 047 (2024), arXiv:2405.18508 [gr-qc].
- [48] K. Destounis, A. G. Suvorov, and K. D. Kokkotas, *Phys. Rev. Lett.* **126**, 141102 (2021), arXiv:2103.05643 [gr-qc].
- [49] F. D. Ryan, *Phys. Rev. D* **56**, 1845 (1997).
- [50] L. Barack and C. Cutler, *Phys. Rev. D* **75**, 042003 (2007), arXiv:gr-qc/0612029.
- [51] A. J. K. Chua, S. Hee, W. J. Handley, E. Higson, C. J. Moore, J. R. Gair, M. P. Hobson, and A. N. Lasenby, *Mon. Not. Roy. Astron. Soc.* **478**, 28 (2018), arXiv:1803.10210 [gr-qc].
- [52] T. Zi and C. Ye, *Phys. Dark Univ.* **48**, 101809 (2025).
- [53] M. Della Rocca, G. Antoniou, L. Gualtieri, and A. Maselli, (2024), arXiv:2412.15131 [gr-qc].
- [54] J. R. Gair, M. Vallisneri, S. L. Larson, and J. G. Baker, *Living Rev. Rel.* **16**, 7 (2013), arXiv:1212.5575 [gr-qc].
- [55] S. Kumar and T. Zi, (2024), arXiv:2412.11847 [gr-qc].
- [56] S. Datta and S. Bose, *Phys. Rev. D* **99**, 084001 (2019), arXiv:1902.01723 [gr-qc].
- [57] L. Meng, Z. Xu, and M. Tang, (2024), arXiv:2411.01858 [gr-qc].
- [58] L. Zhao, M. Tang, and Z. Xu, *Eur. Phys. J. C* **85**, 36 (2025), arXiv:2411.01979 [gr-qc].
- [59] R. Niu, X. Zhang, T. Liu, J. Yu, B. Wang, and W. Zhao, *Astrophys. J.* **890**, 163 (2019), arXiv:1910.10592 [gr-qc].
- [60] C. Zhang, G. Fu, and Y. Gong, (2024), arXiv:2408.15064 [gr-qc].
- [61] J. Tan, J.-d. Zhang, H.-M. Fan, and J. Mei, *Eur. Phys. J. C* **84**, 824 (2024), arXiv:2402.05752 [gr-qc].
- [62] T. Jiang, N. Dai, Y. Gong, D. Liang, and C. Zhang, *JCAP* **12**, 023 (2022), arXiv:2107.02700 [gr-qc].
- [63] E. Barausse, L. Rezzolla, D. Petroff, and M. Ansorg, *Phys. Rev. D* **75**, 064026 (2007), arXiv:gr-qc/0612123.
- [64] E. Barausse and L. Rezzolla, *Phys. Rev. D* **77**, 104027 (2008), arXiv:0711.4558 [gr-qc].
- [65] N. Yunes, B. Kocsis, A. Loeb, and Z. Haiman, *Phys. Rev. Lett.* **107**, 171103 (2011), arXiv:1103.4609 [astro-ph.CO].
- [66] E. Barausse, V. Cardoso, and P. Pani, *Phys. Rev. D* **89**, 104059 (2014), arXiv:1404.7149 [gr-qc].
- [67] C. Zhang and Y. Gong, *Phys. Rev. D* **110**, 104052 (2024), arXiv:2407.07449 [gr-qc].
- [68] Z.-C. Zhang and Y. Tang, *Phys. Rev. D* **110**, 103008 (2024), arXiv:2403.18529 [astro-ph.GA].
- [69] O. A. Hannuksela, K. C. Y. Ng, and T. G. F. Li, *Phys. Rev. D* **102**, 103022 (2020), arXiv:1906.11845 [astro-ph.CO].
- [70] C. Zhang, G. Fu, and N. Dai, *JCAP* **04**, 088 (2024), arXiv:2401.04467 [gr-qc].
- [71] Z.-Y. Tu, T. Zhu, and A. Wang, *Phys. Rev. D* **108**, 024035 (2023), arXiv:2304.14160 [gr-qc].
- [72] Y. Liu and X. Zhang, *JCAP* **10**, 056 (2024), arXiv:2404.08454 [gr-qc].
- [73] S. Yang, Y.-P. Zhang, T. Zhu, L. Zhao, and Y.-X. Liu, *JCAP* **01**, 091 (2025), arXiv:2407.00283 [gr-qc].
- [74] S. Yang, Y.-P. Zhang, T. Zhu, L. Zhao, and Y.-X. Liu, (2024), arXiv:2412.04302 [gr-qc].
- [75] G. Fu, Y. Liu, B. Wang, J.-P. Wu, and C. Zhang, (2024), arXiv:2409.08138 [gr-qc].
- [76] T. Zi and S. Kumar, (2024), arXiv:2409.17765 [gr-qc].
- [77] T. Zi and P.-C. Li, *Phys. Rev. D* **109**, 064089 (2024), arXiv:2311.07279 [gr-qc].
- [78] O. Stashko, *Phys. Rev. D* **110**, 084016 (2024), arXiv:2407.07892 [gr-qc].
- [79] X.-J. Gao, (2024), arXiv:2411.09513 [gr-qc].
- [80] L. A. Sánchez, *Eur. Phys. J. C* **84**, 1056 (2024), arXiv:2408.00226 [gr-qc].
- [81] M. Reuter, *Phys. Rev. D* **57**, 971 (1998), arXiv:hep-th/9605030.
- [82] A. Bonanno, R. Casadio, and A. Platania, *JCAP* **01**, 022 (2020), arXiv:1910.11393 [gr-qc].
- [83] A. Bonanno, T. Denz, J. M. Pawłowski, and M. Reichert, *SciPost Phys.* **12**, 001 (2022), arXiv:2102.02217 [hep-th].
- [84] S. Hopper, C. Kavanagh, and A. C. Ottewill, *Phys. Rev. D* **93**, 044010 (2016), arXiv:1512.01556 [gr-qc].
- [85] C. Cutler, D. Kennefick, and E. Poisson, *Phys. Rev. D* **50**, 3816 (1994).
- [86] P. C. Peters, *Phys. Rev.* **136**, B1224 (1964).
- [87] P. C. Peters and J. Mathews, *Phys. Rev.* **131**, 435 (1963).
- [88] A. J. K. Chua, C. J. Moore, and J. R. Gair, *Phys. Rev. D* **96**, 044005 (2017), arXiv:1705.04259 [gr-qc].
- [89] L. Barack and C. Cutler, *Phys. Rev. D* **69**, 082005 (2004), arXiv:gr-qc/0310125.
- [90] S. Babak, H. Fang, J. R. Gair, K. Glampedakis, and S. A. Hughes, *Phys. Rev. D* **75**, 024005 (2007), [Erratum: *Phys.Rev.D* 77, 04990 (2008)], arXiv:gr-qc/0607007.
- [91] A. J. K. Chua and J. R. Gair, *Class. Quant. Grav.* **32**, 232002 (2015), arXiv:1510.06245 [gr-qc].
- [92] C. Cutler, *Phys. Rev. D* **57**, 7089 (1998), arXiv:gr-qc/9703068.
- [93] T. A. Apostolatos, C. Cutler, G. J. Sussman, and K. S.

- Thorne, Phys. Rev. D **49**, 6274 (1994).
- [94] A. Maselli, N. Franchini, L. Gualtieri, T. P. Sotiriou, S. Barsanti, and P. Pani, Nature Astron. **6**, 464 (2022), arXiv:2106.11325 [gr-qc].
- [95] T. Robson, N. J. Cornish, and C. Liu, Class. Quant. Grav. **36**, 105011 (2019), arXiv:1803.01944 [astro-ph.HE].
- [96] J. Mei *et al.* (TianQin), PTEP **2021**, 05A107 (2021), arXiv:2008.10332 [gr-qc].
- [97] W.-H. Ruan, Z.-K. Guo, R.-G. Cai, and Y.-Z. Zhang, Int. J. Mod. Phys. A **35**, 2050075 (2020), arXiv:1807.09495 [gr-qc].
- [98] E. E. Flanagan and S. A. Hughes, Phys. Rev. D **57**, 4566 (1998), arXiv:gr-qc/9710129.
- [99] L. Lindblom, B. J. Owen, and D. A. Brown, Phys. Rev. D **78**, 124020 (2008), arXiv:0809.3844 [gr-qc].
- [100] M. Vallisneri, Phys. Rev. D **77**, 042001 (2008), arXiv:gr-qc/0703086.
- [101] L. C. Stein and N. Warburton, Phys. Rev. D **101**, 064007 (2020), arXiv:1912.07609 [gr-qc].
- [102] S. Datta, R. Brito, S. Bose, P. Pani, and S. A. Hughes, Phys. Rev. D **101**, 044004 (2020), arXiv:1910.07841 [gr-qc].
- [103] T. Zi and P.-C. Li, Phys. Rev. D **108**, 084001 (2023), arXiv:2306.02683 [gr-qc].
- [104] G. A. Piovano, R. Brito, A. Maselli, and P. Pani, Phys. Rev. D **104**, 124019 (2021), arXiv:2105.07083 [gr-qc].
- [105] G. Franciolini, I. Musco, P. Pani, and A. Urbano, Phys. Rev. D **106**, 123526 (2022), arXiv:2209.05959 [astro-ph.CO].